Delft University of Technology

Effect of the anisotropy of martensitic transformation on ferrite deformation in Dual-Phase steels

Atreya, Vibhor; Van Dokkum, Jan Steven; Bos, C.; Santofimia, Maria J.

DOI
10.1016/j.matdes.2022.110805

Publication date
2022

Document Version
Final published version

Published in
Materials and Design

Citation (APA)
Atreya, V., Van Dokkum, J. S., Bos, C., & Santofimia, M. J. (2022). Effect of the anisotropy of martensitic transformation on ferrite deformation in Dual-Phase steels. *Materials and Design*, *219*, Article 110805. https://doi.org/10.1016/j.matdes.2022.110805

Important note
To cite this publication, please use the final published version (if applicable).
Please check the document version above.

Copyright
Other than for strictly personal use, it is not permitted to download, forward or distribute the text or part of it, without the consent of the author(s) and/or copyright holder(s), unless the work is under an open content license such as Creative Commons.

Takedown policy
Please contact us and provide details if you believe this document breaches copyrights.
We will remove access to the work immediately and investigate your claim.

This work is downloaded from Delft University of Technology.
For technical reasons the number of authors shown on this cover page is limited to a maximum of 10.

Materials & Design 219 (2022) 110805

Contents lists available at ScienceDirect

Materials & Design

journal homepage: www.elsevier.com/locate/matdes

Effect of the anisotropy of martensitic transformation on ferrite deformation in Dual-Phase steels

Vibhor Atreya [a,*], Jan Steven Van Dokkum [a], Cornelis Bos [a,b], Maria J. Santofimia [a]

[a] Department of Materials Science and Engineering, Delft University of Technology, 2628 CD Delft, the Netherlands
[b] Tata Steel, Research & Development, IJmuiden, the Netherlands

HIGHLIGHTS

- The proposed modeling approach estimates martensitic transformation-induced deformation of ferrite in DP steels.
- The anisotropy of transformations is found to be a significant factor determining the deformation of ferrite.
- An influence of PAG orientation and the variant formation on transformation-induced deformation of ferrite is shown.
- This study illustrates an essential step towards a general macroscopic model of plasticity in DP steels.

GRAPHICAL ABSTRACT

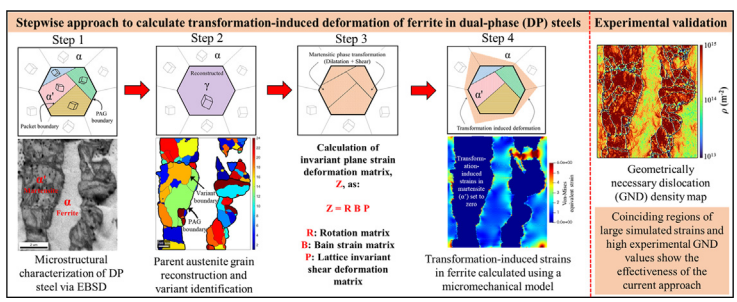

ARTICLE INFO

Article history:
Received 24 March 2022
Revised 18 May 2022
Accepted 29 May 2022
Available online 31 May 2022

Keywords:
Dual-phase steel
Martensitic transformation
Electron backscatter diffraction
Plastic deformation
Martensite variants
Micromechanical modeling

ABSTRACT

The volume increase and shape change during austenite to martensite transformation in dual-phase (DP) steels are largely accommodated in the microstructure by the deformation of the surrounding ferrite matrix. Accurate estimation of transformation-induced deformation of ferrite via experiments and modeling is essential for predicting the subsequent mechanical behavior of DP steels. This study aims to illustrate the disadvantages of simplifying the anisotropic transformation deformation of martensite to isotropic dilatation for modeling the transformation-induced deformation of ferrite. A novel methodology is developed comprising sequential experimental and numerical research on DP steels to quantify transformation-induced strains in ferrite. This methodology combines the results of prior austenite grain reconstruction, phenomenological theory of martensite crystallography and electron backscatter diffraction (EBSD) orientation data to estimate variant-specific transformation deformation. Subsequently, by comparison of full-field micromechanical calculation results on a virtual DP steel microstructure with experimental EBSD kernel average misorientation and geometrically necessary dislocation measurement results it is shown that neglecting the shear deformation associated with the martensitic transformation leads to significant underestimation in the prediction of transformation-induced strains in ferrite.

© 2022 The Author(s). Published by Elsevier Ltd. This is an open access article under the CC BY license (http://creativecommons.org/licenses/by/4.0/).

1. Introduction

The microstructure of dual-phase (DP) steels consists of hard martensite embedded in a soft ferritic matrix, which provides DP steels with a good combination of strength and ductility. As a

* Corresponding author.
E-mail address: V.Atreya@tudelft.nl (V. Atreya).

https://doi.org/10.1016/j.matdes.2022.110805
0264-1275/© 2022 The Author(s). Published by Elsevier Ltd.
This is an open access article under the CC BY license (http://creativecommons.org/licenses/by/4.0/).

result, DP steels find widespread use in the automobile sector [1–3]. The martensite present in the microstructure of DP steels is typically formed when austenite present in the microstructure at intercritical condition transforms into martensite upon rapid cooling. The intercritical ferrite does not undergo any phase transformation during such an operation.

The austenite to martensite phase transformation is accompanied by a volume increase and a shape change [4,5]. Macroscopically, this is observed as a unidirectional dilatation and shear deformation of the transforming region. To accommodate the newly formed martensite in the microstructure, the ferritic matrix also undergoes deformation. The resulting local stresses in ferrite exceed the elastic limit, which results in plastic flow and subsequent strain hardening [6,7].

The transformation-induced plastic deformation of ferrite generates a high density of unpinned dislocations near the ferrite/martensite interface [8–10]. Because of the high local stresses already present in the ferrite matrix, the newly formed dislocations start to move and interact even at a relatively low value of global flow stress [11,12], which results in the typical characteristics of DP steels such as a low elastic limit, continuous yielding, and a high initial work hardening rate [13,14]. Moreover, the extent of transformation-induced deformation of ferrite significantly influences the yield strength and hardening behavior of DP steels [6,7], which highlights the need of estimating the transformation-induced deformation of ferrite to understand the global mechanical behavior of DP steels.

Until now, only indirect qualitative experimental studies have been performed to estimate the transformation-induced deformation of ferrite. These include estimating the extent of ferrite deformation by measuring the lattice misorientations by electron backscatter diffraction (EBSD) [1,15–17], and nanoindentation measurements near the ferrite/martensite interface to measure the ferrite strain hardening due to martensitic transformation [1,16,18]. Direct measurement of transformation-induced deformation of ferrite is challenging owing to the fact that martensitic transformation occurs at a very high rate due to its displacive nature.

Continuum mechanics based analytical models for transformation-induced deformation of ferrite have been formulated for regular shaped martensite islands [11,12]. While Sakaki et al. [11] estimated the spatial extent of plastic deformation, Bourell and Rizk [12] estimated the dislocation density increase in the deformed ferrite matrix surrounding a spherical martensite island. For microstructures consisting of martensite with more complex shapes, the transformation-induced deformation of ferrite has been described with a micromechanics based numerical modeling approach [6,7,18]. The anisotropic character of the transformation deformation, which comprises of shear and dilatation deformation accompanying the formation of every martensitic variant from a prior austenite grain (PAG), can be expected to have a strong influence on the transformation-induced deformation of ferrite. However, in the aforementioned works, the transformation deformation was assumed to be comprised only of isotropic dilatation of the prior austenite grains.

The assumption of isotropic dilatation implies that the shear deformation associated with the formation of martensitic variants, oriented differently in space, cancel each other out leaving only the unidirectional dilatation part for consideration. The volume average deformation of all variants combined is then considered equivalent to the isotropic dilatation of the PAG. This assumption is reasonable when the prior austenite grain size is sufficiently large to allow the formation of a maximum of twenty-four martensitic variants with different orientations. However, in the case of DP steels, the small prior austenite grain size (PAGS) allows only the formation of a few martensitic variants [19–21]. Hence the volume average shear of all variants is non-zero, and the volume average deformation of all variants combined is less likely to be equal to the isotropic dilatation of the PAG.

This study aims to show the disadvantages of simplifying the anisotropic transformation deformation of martensite to isotropic dilatation for studying the transformation-induced deformation of ferrite in the case of relatively small PAGS, such as in DP steels. Subsequently, quantification of the transformation-induced deformation of ferrite is proposed using a novel methodology comprising sequential experimental and numerical research on DP steels.

2. Approach and theoretical models

The approach to model the transformation-induced deformation of ferrite is schematically presented in Fig. 1. It is divided into four steps and starts with an EBSD scan of the DP steel microstructure to obtain lattice orientations of ferrite and martensite, followed by prior austenite grain reconstruction to estimate the morphology and lattice orientation of prior austenite grains. The anisotropic transformation deformation is then determined by using the phenomenological theory of martensite crystallography (PTMC) [5,22,23]. As per the authors' knowledge, the application of a crystallographic theory (such as the PTMC) to calculate the magnitude of shear and dilatation components of transformation deformation is missing in the previous modeling works concerning the transformation-induced deformation of ferrite in DP steels. Subsequently, the transformation is mimicked by subjecting all reconstructed prior austenite grains, constrained by an initially undeformed ferrite matrix, to the anisotropic deformation associated with the transformation. The resulting transformation-induced deformation of ferrite is calculated using a micromechanical model (Appendix A) [24]. The detailed explanation of every step follows.

2.1. Analysis of the ferrite/martensite microstructure (Step 1)

The EBSD scan of a selected location within the DP steel specimen is carried out to obtain information about the distribution of phases and crystal orientations. Although both ferrite and martensite are recognized in the EBSD as bcc crystal structures, martensite regions exhibit low image quality in the EBSD scans. Therefore the grain average image quality measure is used to distinguish martensite from ferrite regions [25]. The identified martensite data points are used as input for the PAG reconstruction.

2.2. Prior austenite grain reconstruction (Step 2)

The most well-known orientation relation observed between austenite and martensite is the Kurdjumov-Sachs (K-S) orientation relationship (OR). However, the experimentally observed OR usually deviate from the ideal K-S OR [26]. Therefore it is necessary to determine the observed OR in the specimen under study.

The misorientation matrix, $\mathbf{M}_{ij}$, between two martensitic variants, i and j, formed from the same prior austenite grain can be represented as [27,28]

$$\mathbf{M}_{ij} = \mathbf{C}_j^{-1}\,\mathbf{T}^{-1}\,\mathbf{S}_j^{-1}\,\mathbf{S}_i\,\mathbf{T}\,\mathbf{C}_i\,, \tag{1}$$

where $\mathbf{S}_i$ and $\mathbf{S}_j$ are one of the 24 cubic symmetry matrices for the prior austenite grains of ith and j^{th} martensitic variants respectively, $\mathbf{C}_i$ and $\mathbf{C}_j$ are one of the 24 cubic symmetry matrices for i^{th} and j^{th} martensitic variants as well, $\mathbf{T}$ is the austenite-martensite orientation relationship matrix, and superscript $\bullet^{-1}$ denotes the inverse. Here, the subscripts are not index notations. The term $\left(\mathbf{T}^{-1}\,\mathbf{S}_j^{-1}\,\mathbf{S}_i\,\mathbf{T}\right)$ results in 24 distinct rotations [27]. If the experimentally observed misorientation matrix $\mathbf{M}_{\text{exp}}$, between the two

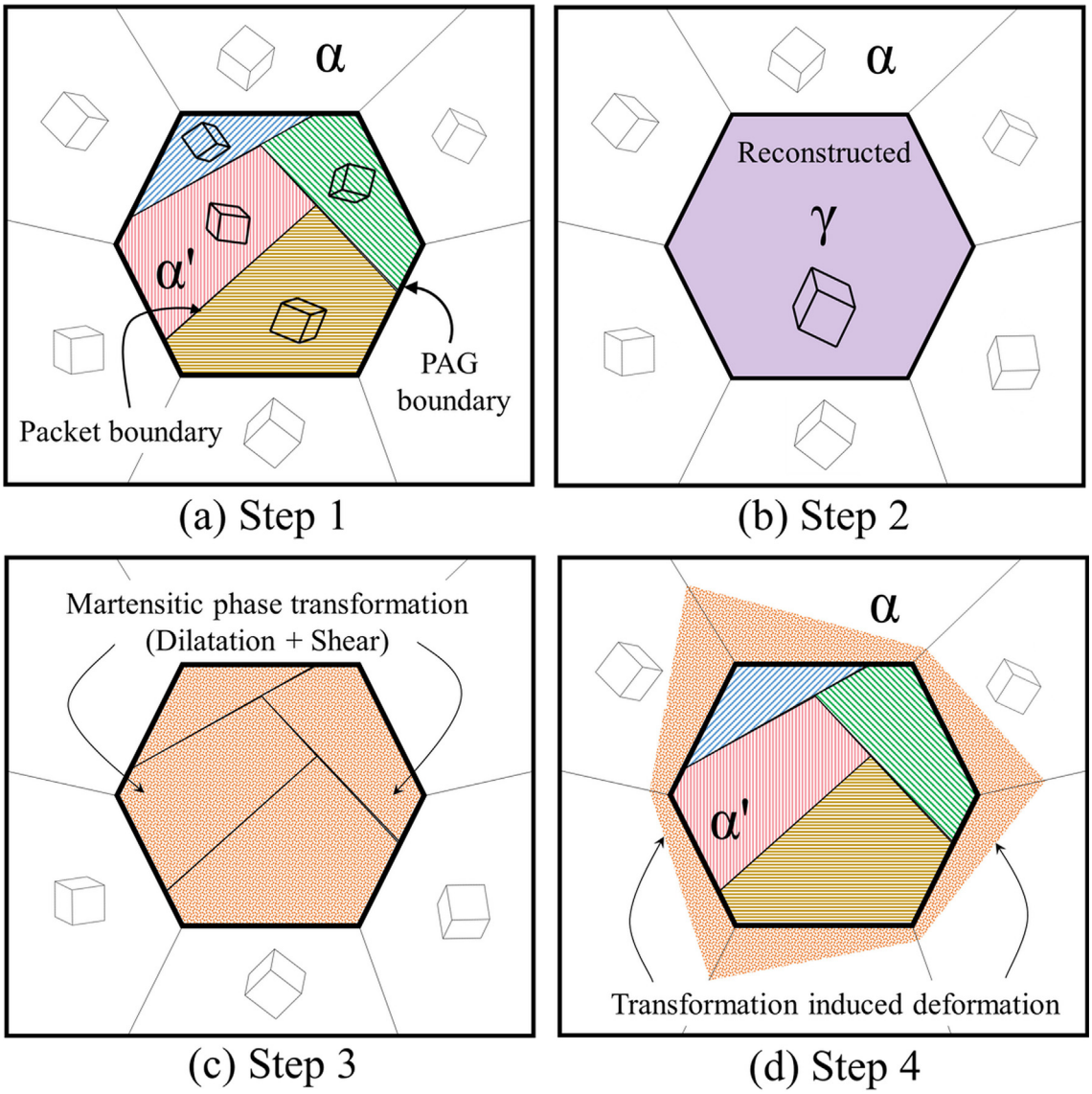

Fig. 1. Illustration of the four steps involved in the calculation of transformation-induced deformation of ferrite. (a) The crystal orientations of ferrite and martensite phases in the specimen are obtained from EBSD measurements (b) A PAG reconstruction algorithm provides the shape and the crystal orientation of the PAGs. (c) The anisotropic transformation deformations are calculated using the phenomenological theory of martensite crystallography (PTMC) (d) The reconstructed PAGs are subjected to the calculated anisotropic and variant-specific transformation deformations and the resulting transformation-induced deformation of ferrite is calculated via micromechanical modeling.

martensitic variants, i and j, is found to be close to one of the predicted 24^3 misorientation matrices according to Eq. 1, the two variants are assigned to the same PAG. However, prior to this calculation, the OR matrix $\mathbf{T}$ should be ascertained. Manipulating Eq. 1, we find that:

$$\mathbf{T} = \left(\mathbf{T}^{-1}\,\mathbf{S}_j^{-1}\,\mathbf{S}_i\right)^{-1}\mathbf{C}_j\,\mathbf{M}_{\exp}\,\mathbf{C}_i^{-1}\,. \tag{2}$$

Since the OR matrix $\mathbf{T}$ appears on both sides of Eq. 2, the equation can only be solved iteratively. Eq. 2 then becomes:

$$\mathbf{T}_{n+1} = \left(\bar{\mathbf{T}}_n^{-1}\,\mathbf{S}_j^{-1}\,\mathbf{S}_i\right)^{-1}\mathbf{C}_j\,\mathbf{M}_{\exp}\,\mathbf{C}_i^{-1}\,, \tag{3}$$

where n is the iterator, $\mathbf{T}_{n=0}$ is the initial guess for $\mathbf{T}_n$ equal to the OR matrix corresponding to the theoretical K-S OR, $\mathbf{T}_{n+1}$ is the OR matrix calculated from $\mathbf{M}_{\exp}$, and $\bar{\mathbf{T}}_n$ is the OR matrix corresponding to average of all ORs determined in the previous iterations. The iterative process is based on determining correct symmetry matrices by using $\mathbf{T} = \bar{\mathbf{T}}_n$ in Eq. 1 and comparing all predicted values of misorientation matrix $\mathbf{M}_{ij}$ with $\mathbf{M}_{\exp}$. When there is no change in the calculated symmetry matrices in subsequent iterations, the final OR matrix $\bar{\mathbf{T}}_n$ is concluded to be the observed experimental orientation relationship for the specimen under study.

The application of this reconstruction algorithm not only predicts the PAG shape but also helps in identifying the martensitic variants and provides an estimate for PAG crystal orientation. This information is further used to determine the anisotropic, variant-specific transformation deformation.

2.3. Determination of martensitic transformation deformation (Step 3)

The austenite to martensite phase transformation comprises of dilatation and shear deformation [5,22,29]. The transformation is an invariant plane strain (IPS) deformation, where the invariant plane is also called the habit plane. The dilatation part is perpendicular to the invariant plane of martensitic transformation, while

the shear part is parallel to the invariant plane. According to the phenomenological theory of martensite crystallography (PTMC), the IPS can be expressed in the form of the following equation [23,5,22]:

$$\mathbf{Z} = \mathbf{R}\,\mathbf{B}\,\mathbf{P}, \tag{4}$$

where $\mathbf{Z}$ is the IPS shape deformation gradient matrix, $\mathbf{R}$ is the rotation matrix representing a rigid body rotation, $\mathbf{B}$ is the bain strain matrix, and $\mathbf{P}$ is the lattice invariant shear matrix. The lattice invariant shear is either in the form of slip, resulting in the formation of laths in low carbon martensite, or in the form of twinning in high carbon martensite [30]. Since martensitic transformation is an invariant plane strain deformation, $\mathbf{Z}$ can also be written in the following form [29]

$$\mathbf{Z} = \mathbf{I} + m\,\hat{d} \otimes \hat{p}, \tag{5}$$

where m is the magnitude of displacements in the direction of displacement unit vector $\hat{d}, \hat{p}$ is the habit plane unit normal vector, and $\otimes$ is the outer product. The slip plane and direction for the lattice invariant shear matrix $\mathbf{P}$ are assumed to be $\{1\,1\,2\}1\,1\,1_{\mathrm{bcc}}$ since it is common to observe $\{1\,1\,2\}$ striations on the martensite surface [31]. The shape deformation gradient matrix $\mathbf{Z}$ and the rotation matrix $\mathbf{R}$ are now calculated from Eqs. 4 and 5. The bain strain matrix $\mathbf{B}$ is calculated from lattice parameters of martensite and prior austenite [29]. In this work, PTC lab software [32] is used to obtain the solution for the shape deformation gradient matrix $\mathbf{Z}$ by providing lattice parameters of austenite and martensite as inputs.

Apart from the shape deformation gradient matrix $\mathbf{Z}$, the PTMC also enables the calculation of orientation transformation matrix $\mathbf{T}$ using the PTC lab software [32]. The change in crystallographic orientation due to martensitic transformation can be expressed in the form of the following matrix equation [33,34]:

$$\mathbf{M} = \mathbf{T}\,\mathbf{A}, \tag{6}$$

where $\mathbf{M}$ and $\mathbf{A}$ are the orientation matrices consisting of three orthogonal unit vectors representing the crystal orientation of martensite and austenite respectively. The orientation transformation matrices of all 24 K-S variants of martensite are

$$\mathbf{T}_k = \mathbf{C}_k\,\mathbf{T}\,\mathbf{C}_k^{\mathrm{T}}, \tag{7}$$

where $\mathbf{C}$ is the cubic symmetry matrix, $k = 1\cdots24$, and $\bullet^T$ is the transpose of the matrix. Plugging Eq. 7 into 6, we have

$$\mathbf{M}_k = \mathbf{C}_k\,\mathbf{T}\,\mathbf{C}_k^{\mathrm{T}}\,\mathbf{A}, \tag{8}$$

which gives the orientation matrices of all 24 variants formed from a prior austenite grain. Similarly, the IPS solution $\mathbf{Z}$ for all 24 variants formed from a single prior austenite grain is calculated using the following equation:

$$\mathbf{Z}_k = \mathbf{C}_k\,\mathbf{Z}\,\mathbf{C}_k^{\mathrm{T}}, \tag{9}$$

where $\mathbf{Z}_k$ is the variant-specific deformation matrix which can only be obtained if the correct symmetry matrix $\mathbf{C}_k$ is identified. The symmetry matrix $\mathbf{C}_k$ which results in the minimum misorientation angle between $\mathbf{M}_k$ and the experimentally measured orientation matrix of a variant is concluded to be the correct symmetry matrix for that variant present at a specific martensite location in the EBSD scan.

The deformation gradient matrix $\mathbf{Z}_k$ is calculated with respect to the reference frame of the prior austenite grain. Any given PAG has an arbitrary orientation with respect to the specimen coordinates. The correct IPS deformation gradient matrix for any martensitic variant is [35]:

$$\mathbf{Z}_{kl} = \mathbf{A}_l\left(\mathbf{C}_k\,\mathbf{Z}\,\mathbf{C}_k^{\mathrm{T}}\right)\mathbf{A}_l^{\mathrm{T}}, \tag{10}$$

where $\mathbf{A}_l$ is the orientation matrix of lth prior austenite grain. The variant-specific deformation gradient matrices, $\mathbf{Z}_{kl}$, are used to calculate the variant-specific eigenstrains ϵ^*_{kl}. Eigenstrains are the strains developed in the material due to the inelastic processes such as phase transformation and thermal expansion in the absence of any external mechanical stress. The variant-specific eigenstrains ϵ^*_{kl} are then used as input in micromechanical model to calculate the transformation-induced strains in ferrite.

2.4. Micromechanical calculation of transformation-induced strains in ferrite (Step 4)

In the last step of the proposed procedure, micromechanical calculations are performed to estimate the transformation-induced strains in ferrite matrix in response to austenite undergoing variant-specific deformation while transforming into martensite. A fast fourier transform based micromechanical model is used to perform the calculations (Appendix A.1) [24]. The inputs for the calculations are: a representative volume element (RVE) based on a microstructural image of DP steel, a behavior law for each phase involved in the RVE, the boundary conditions imposed on the RVE, and the eigenstrains corresponding to martensitic transformation deformation.

In the present micromechanical model calculations, the strains are assumed to be infinitesimal. This means that the second-order terms from the definition of finite strain are neglected. Therefore any significant transformation-induced rotation in the material contributes to the error in calculated transformation-induced strains. A comparative analysis of the transformation-induced deformation of ferrite is performed, in response to two different assumptions regarding martensite transformation deformation. The trends observed are considered representative given the absence of local *a priory* known rotations. The intention here is to use the simplest numerical method to elucidate the importance of a key aspect of martensitic transformation.

3. Analysis of a DP steel microstructure using the proposed method

3.1. Experimental procedure

A cold-rolled steel with composition Fe-0.14C-1.8Mn-0.24Si by weight % and with an initial microstructure consisting of pearlite and ferrite was cut into a specimen of dimensions 10 mm × 4 mm × 2 mm using electrical discharge machining. Using a Bähr DIL A/D dilatometer, the specimen was heated at 5 K/s, kept at 1048 K for 5 min, and then quenched to obtain a ferrite-martensite dual-phase microstructure. The specimen was ground using SiC abrasive papers and subsequently polished using 3 and 1 μm diamond paste. Further, it was electropolished using Struers A2 electrolyte at 35 V, 277 K for 6 s. EBSD measurements were made on a Zeiss Ultra 55 scanning electron microscope (SEM) using the Edax Pegasus XM 4 Hikari EBSD system. The step size of the scan was 50 nm. The EBSD scans were analyzed using the TSL OIM version 7 software.

3.2. Application

3.2.1. Analysis of the ferrite/martensite microstructure

The microstructure of the specimen used in this work was investigated in detail in a previous study [36]. Fig. 2(a) shows the image quality (IQ) map of the specimen obtained via EBSD scan. The dark-colored martensite is present in the form of connected,

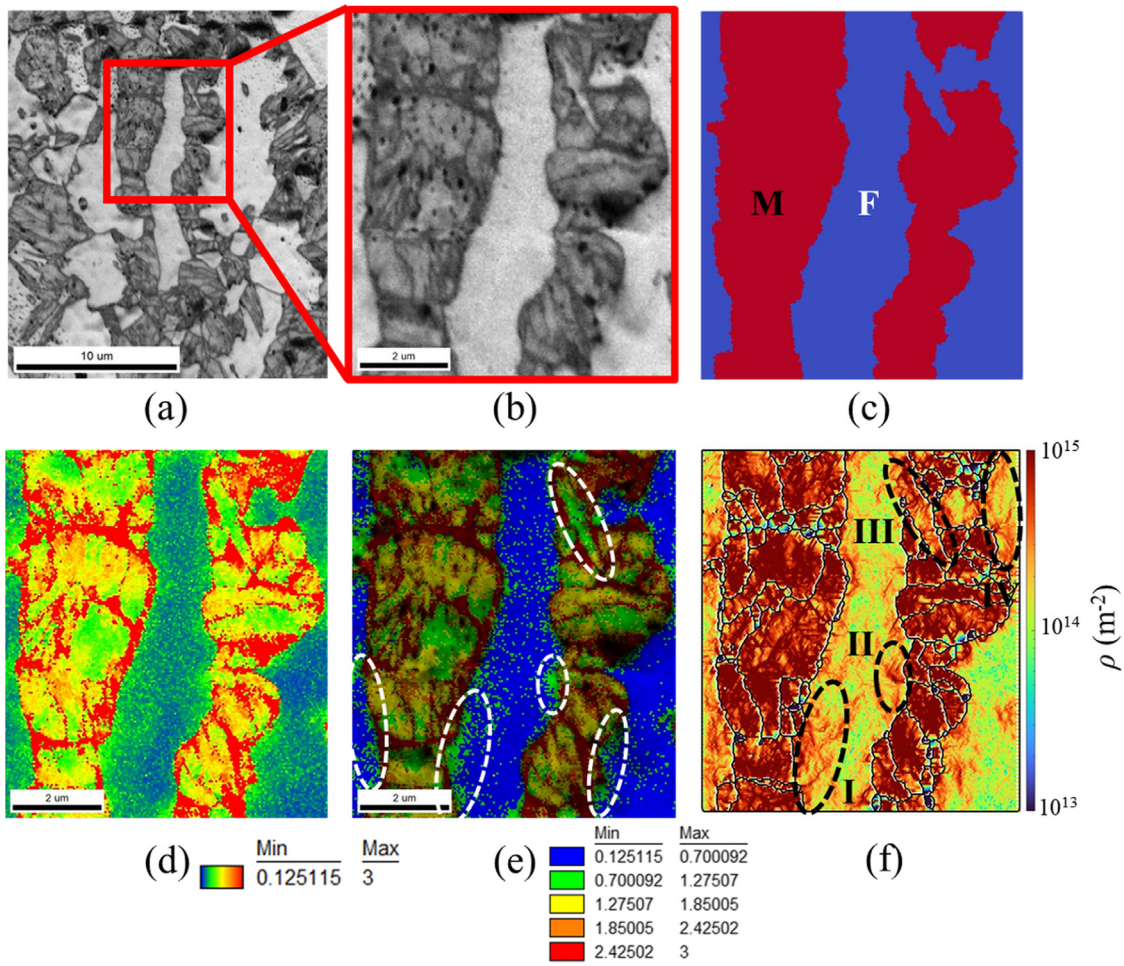

Fig. 2. (a) Image quality (IQ) map of the specimen region scanned with EBSD (b) Specific area selected for this study (c) Generation of an RVE consisting of ferrite and martensite (d) Kernel average misorientation (KAM) map for the selected region. KAM values are in degrees (e) KAM map for the selected region with values grouped into specific ranges. Areas within white dashed white ellipses indicate higher KAM regions in ferrite (f) Geometrically necessary dislocations (m^{-2}) calculated for the region of interest. Some regions of higher GND density are highlighted with black dashed ellipses.

chain-like structures. The region used for PAG reconstruction and RVE generation for micromechanical calculations is highlighted in red and shown enlarged in Fig. 2(b). The RVE hence generated is shown in Fig. 2(c) where blue and red colors represent ferrite and martensite respectively.

The martensite volume fraction for the specific scanned location of the specimen was calculated to be 0.56 [36], based on phase identification using grain average image quality (GAIQ) measurements [25,36]. GAIQ is the average image quality of all measurement points within a grain. Using an angular tolerance value between 0.5 and 1.5°to identify the grains followed by an application of GAIQ measure enables excellent identification and quantification of martensite in a DP steel microstructure [25,36]. The equilibrium carbon content in ferrite at the intercritical temperature calculated using ThermoCalc software is 0.006 wt%. Consequently, the carbon content in martensite was calculated to be 0.23 wt% [34] after the application of carbon mass balance. The lattice parameters used in this study are a = 2.858 nm and c = 2.885 nm for martensite and a = 3.565 nm for prior austenite based on calculated carbon content [37].

The nth neighbor kernel average misorientation (KAM) at an EBSD measurement point is the average misorientation of the nth nearest neighbor points with respect to that measurement point. Since intra-grain misorientations arise due to dislocations, and KAM values can be used to study the level of deformation within individual grains [38]. Fig. 2(d) shows the KAM maps of the region of interest for the 5th nearest neighbors and a maximum 3° misorientation. As expected, the highest KAM values are observed for the martensite regions. The KAM magnitude is higher in ferrite grains near the phase boundary than in the grain interior. This becomes apparent in Fig. 2(e), where the KAM values are grouped into five uniformly spaced ranges and overlaid on the IQ map. The regions near the phase boundary which show higher KAM are highlighted in dashed white ellipses.

A local geometrically necessary dislocation (GND) density map is calculated using MTex software [39–41], following the approach given by Pantleon [42]. This approach involves the calculation of dislocation density tensor at every measurement point of the EBSD scan, whose components are determined using the lattice curvature tensor. The lattice curvature tensor is calculated from the misorientations between neighboring points in an EBSD scan. Fig. 2(f) shows the result for the GND density calculations, with some regions of relatively high GND densities highlighted with black dashed ellipses.

3.2.2. Prior austenite grain reconstruction

To carry out the prior austenite grain (PAG) reconstruction, the bcc ferrite phase data points in the EBSD maps were identified using the grain average image quality (GAIQ) criterion and then removed from the EBSD scan data. Reconstruction was then per-

formed on the remaining martensite data points. Mtex version 5.6 toolbox available in Matlab [39] was used for carrying out the PAG reconstruction.

Fig. 3(a) shows the reconstructed parent grain boundaries overlaid on the IQ map of the region of interest shown in Fig. 2(b). Figs. 3(b) and 3(c) show the packet and variant map of all the PAGs shown in Fig. 3(a). The PAGs are very small and with a mean diameter of 1.6 μm and the average number of variants in a PAG is 6.

Fig. 4(a) shows the pole figure orientation of the largest prior austenite grain, named 'PAG 1', indicated in Fig. 3(a). Fig. 4(b) shows the pole figures of identified variants of 'PAG 1'. The theoretical pole figure of all 24 variants according to the OR identified during the reconstruction is shown in Fig. 4(c). Experimental pole figures of the variants match very well with the expected theoretical pole figures. The experimental OR was found to be 1.1 degrees off from theoretical K-S relationship.

A comparison of the pole figures of martensitic variants according to theoretical K-S OR and those obtained via PTMC is shown in Fig. 4(d). The misorientation between predictions of variant orientation by K-S OR and that by PTMC is 3.22°. Neither the PTMC nor the K-S OR predicts the experimentally observed ORs accurately.

As per the prediction of PTMC, the deviation between close-packed planes of austenite $(111)_\gamma$ and martensite $(110)_\alpha$ decreases from 0.4° to 0.3° when the carbon content increase from 0.1 wt% to 0.4 wt%. This is also corroborated in experiments where the decrease in angular deviation for close-packed planes is from 0.8° to 0.3° for the same increase in carbon content [43]. This shows that even though PTMC may not capture the experimentally observed OR, it can predict the changes in OR with varying carbon content in austenite/martensite.

3.2.3. Determination of martensitic transformation deformation

The anisotropic transformation eigenstrain for martensite, $\epsilon^{*,\text{aniso}}_{kl}$, for the kth variant of the lth austenite grain is calculated from the anisotropic transformation deformation matrix, $\mathbf{Z}_{kl}$ of Eq. 9 using the definition of Green-Lagrange strain (appendix A.1). The value of m in Eq. 5 as calculated using PTMC theory is 0.26. The transformation eigenstrain matrix for isotropic dilatation of martensite, $\epsilon^{*,\text{iso}}$, is of the form $\epsilon^{*,\text{iso}} = (\Delta/3)\,\delta_{ij}$, where Δ is the volumetric strain for austenite to martensite transformation and δ_{ij} is the Kronecker delta representing the identity matrix. The volumetric strain accompanying martensitic phase transformation depends on the carbon content as [4,11]:

$$\Delta = \left(\frac{\Delta V_{\gamma\to\alpha}}{V_\gamma}\right)_{M_s} = 0.017 + 0.013X_C\,, \tag{11}$$

where $\Delta V_{\gamma\to\alpha}$ is the change in specific volume due to phase transformation from austenite (γ) to martensite (α), V_γ is the specific volume of austenite, and X_C is the carbon content of austenite in wt%. For $X_C = 0.23$, Δ is calculated to be 2.0×10^{-2}. In Eq. 11, all transformation is assumed to occur at the martensite start temperature (M_S).

3.2.4. Micromechanical calculation of transformation-induced strains in ferrite

Following PAG reconstruction, the micromechanical model calculations are performed on the EBSD-based RVE to calculate transformation-induced strains in ferrite. Depending upon the variant identity, the corresponding eigenstrain is applied at the locations of transformation. The lattice-invariant shear between the martensitic laths is a part of the macroscopic shape deformation, and therefore does not need to be considered separately in the micromechanical calculations. Assuming a fixed room-temperature value of linear thermal expansion coefficient, the thermal strain in ferrite due to quenching is in the order of 10^{-3} [44]. The strains induced in ferrite by anisotropic martensitic transformations are expected to be higher in magnitude (in the order of 10^{-1}) than the thermal strains, hence thermal strains are not considered in this study.

The material behavior of martensite was assumed to be isotropic elastic, while ferrite was considered isotropic elastic-plastic with linear hardening in the following form:

$$\sigma_0 = \sigma_Y + H\epsilon_{vM}\,, \tag{12}$$

where σ_0 is the flow stress, σ_Y = 283 MPa is the uniaxial ferrite yield strength, H = 595 MPa is the plastic modulus [24]-a parameter which determines the level of strain hardening depending upon strain magnitude and ϵ_{vM} is von-Mises equivalent strain. The values of σ_Y and H were chosen in such a way that the flow curve resulting from Eq. 12 is the best linear fit for the experimentally observed uniaxial tensile flow curve of ferrite with a similar carbon concentration as shown in Fig. 5 [45]. The elastic modulus and Poisson's ratio for martensite (E = 203.5 GPa, ν = 0.292) and ferrite (E = 209 GPa, ν = 0.289) are obtained from the literature [46].

For the EBSD based RVE, the spatial discretization in the x, y and z directions is 332 × 291 × 1, equal to the number of measurement

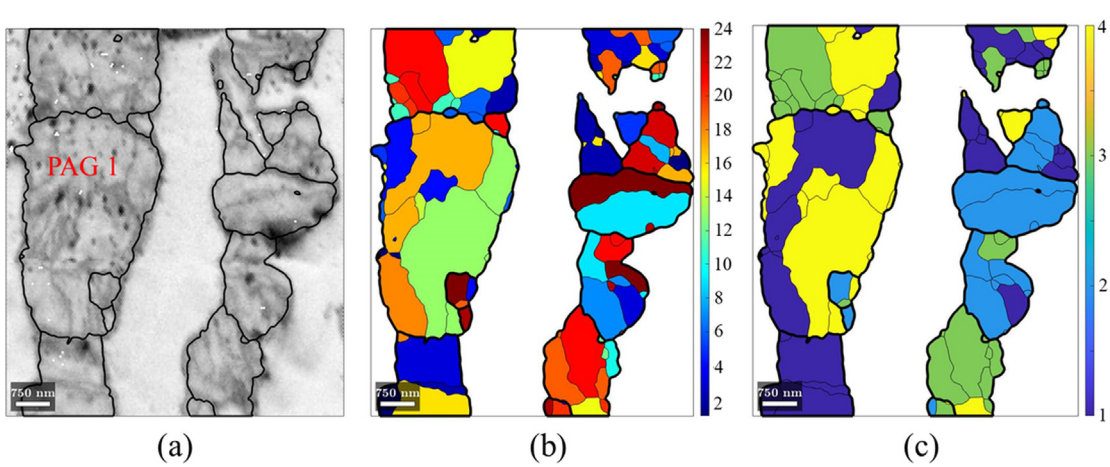

Fig. 3. (a) Reconstructed prior austenite grain boundaries in black overlaid on image quality map of the region of interest (b) Variants of every PAG coloured differently, with a maximum of 24 variants per PAG (c) Packets of every PAG coloured differently, with a maximum of 4 packets per PAG.

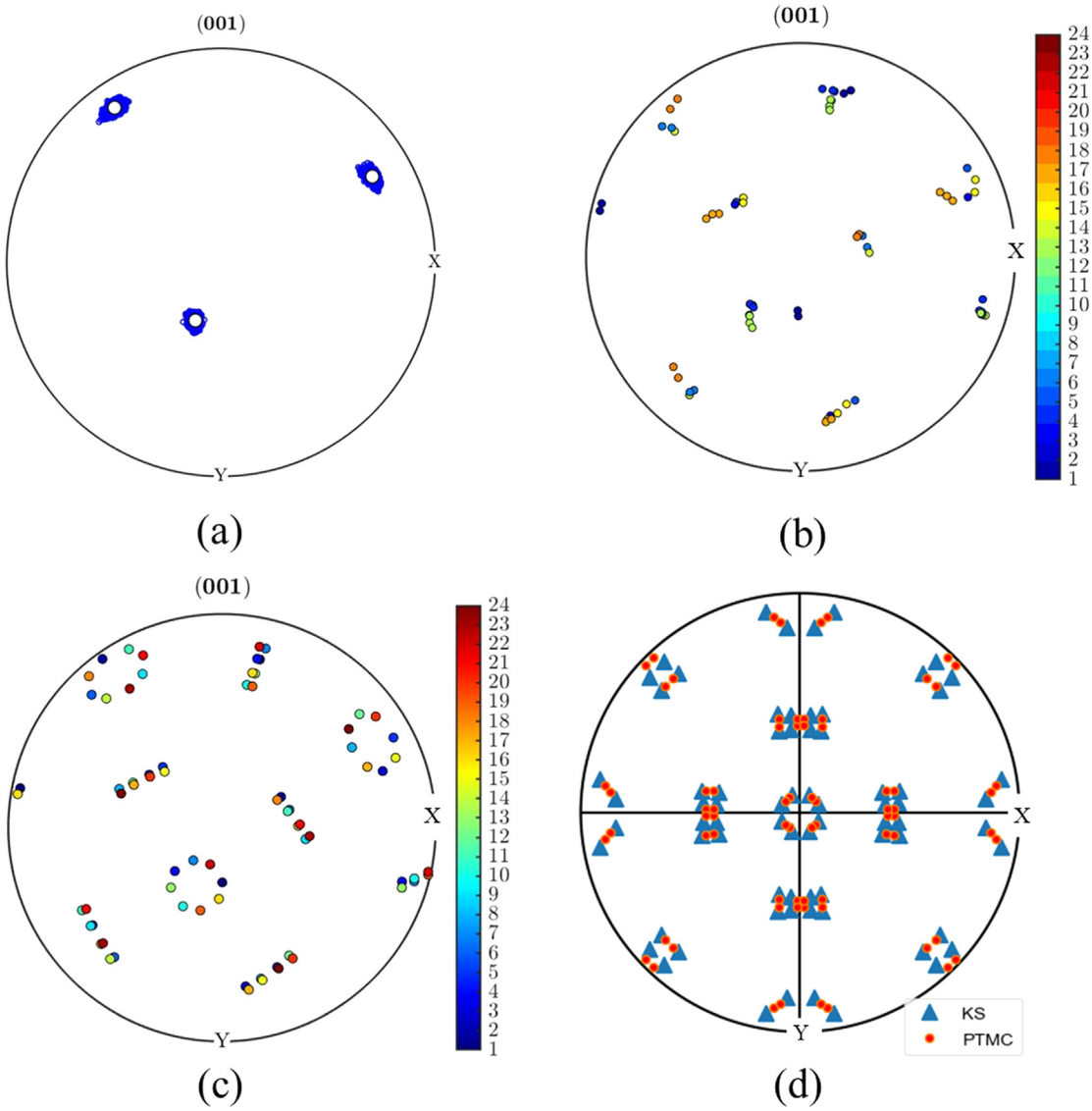

Fig. 4. (a) Pole figure of the largest prior austenite grain (PAG 1) indicated in Fig. 3(a); (b) The pole figures of identified variants. (c) The theoretical pole figure of all 24 variants according to the OR identified during the reconstruction (d) A comparison of the pole figures of martensitic variants according to theoretical K-S OR and those obtained via PTMC.

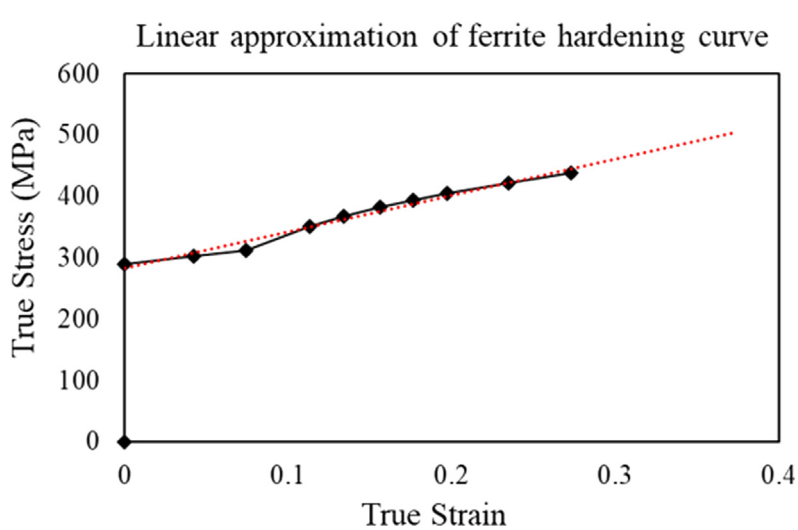

Fig. 5. (a) Linear approximation of ferrite hardening curve (in red dotted line) based on experimental flow curves of ferrite presented in reference [45].

points in the area selected to study from the EBSD scan. Periodic boundary conditions are applied in the plane of the 2D surface. No information is available on grain morphology out of the plane. Therefore, a mechanical limit is applied and the average far-field strain orthogonal to the 2D surface is set to zero, i.e., plane strain condition was considered for the in-plane direction. The convergence of the numerical iterative process was evaluated by comparison with the required accuracy of 10^{-5} m^{-1}.

Fig. 6 shows the von-Mises equivalent map of (a) transformation-induced strains in ferrite due to isotropic transformation eigenstrains, $\epsilon_{vM}^{iso,tr\text{-}ind}$, and (b) transformation-induced strains in ferrite due to anisotropic transformation eigenstrains, $\epsilon_{vM}^{aniso,tr\text{-}ind}$. The magnitude of deformation at all locations in ferrite is found to be higher in Fig. 6(b) than in 6(a). The high strain regions highlighted with black dashed circles at the top and bottom edge of both Figs. 6(a) and 6(b), arise because of the imperfect periodicity of the microstructural region selected for this study. It is to be noted that the elastic lattice strains within martensite are numerically obtained but are not shown in the strain maps as they hamper the visibility of strains in ferrite.

4. Discussion

Figs. 2(d) and 2(e) show that some regions of ferrite near the phase boundary have higher KAM values, indicating higher deformation. These regions are highlighted by dashed white ellipses in Fig. 2(e). As per the literature, the spatial extent of ferrite deformation lies approximately in the range of 0.1 μm–0.5 μm from the ferrite/martensite interface [36]. It is important to note that this distance is not a single fixed value. Previous micromechanical modeling studies assuming isotropic dilatation during transformation conclude that a continuous deformed ferrite region of specific width exists along the phase boundaries [6,7,18]. The results of the present modeling study, shown in Fig. 6(a) and 6(b), corroborate previous experimental results that the deformed ferrite region is discontinuous and the extent of deformation varies from one location to another [36].

The PAG reconstruction results shown in Fig. 3 reveal that the PAGs in the current DP steel specimen are very small with a mean diameter of 1.6 μm and an average of 6 variants within every PAG. As mentioned earlier, several previous studies assumed that the shear component of transformation for differently oriented variants cancel each other leaving only the dilatation part as the effective transformation deformation [6,7,11,12]. However, present results suggest that such an assumption should be avoided wherever small PAGs with much less than 24 variants are present. For instance, the prior austenite grain marked 'PAG 1' in Fig. 3(a) consist of 14 variants. The magnitude of ferrite deformation adjacent to 'PAG 1' for the case of isotropic dilatation (Fig. 6(a)) is less than that of anisotropic deformation (Fig. 6(b)). This proves that the shear deformations accompanying the formation of 14 variants do not cancel out, otherwise, the transformation-induced deformation of ferrite would have been similar in both cases. Therefore, the average transformation deformation in DP steels with small PAGS cannot be considered equivalent to an isotropic dilatation of prior austenite.

The micromechanical model calculation results in Figs. 6(a) and 6(b) show that the transformation-induced deformation of ferrite is non-homogenous throughout the microstructure, regardless of the assumption of isotropic or anisotropic transformation deformation. This non-homogeneity is more pronounced in Fig. 6(b) since the variation in magnitude of transformation-induced strains is larger in this case. For example, the strain in the region marked '1' is a lot higher in magnitude compared to that of the region marked '2'.

The assumption of isotropic or anisotropic transformation deformation in the micromechanical calculations affects the distribution of transformation-induced strains in ferrite. Large strains are present at different locations depending on the choice of the assumption. For instance, in Fig. 6(b), the area marked '3' shows relatively large strain compared to its surroundings, whereas in Fig. 6(a) the same area shows comparatively smaller strain. Similarly, the areas marked '4' and '5' also show relatively large strain in Fig. 6(b) than in Fig. 6(a). In general, at most locations, the strain in ferrite due to anisotropic transformation deformation is larger by a factor of up to 10 times than that induced by isotropic dilatation.

In the case of isotropic transformation deformation, the dilatation is the same for all the variants. Therefore the non-homogeneity in the transformation-induced deformation of ferrite, in this case, is because of complex grain shapes. In the case of anisotropic transformation deformation, the non-homogeneity in the

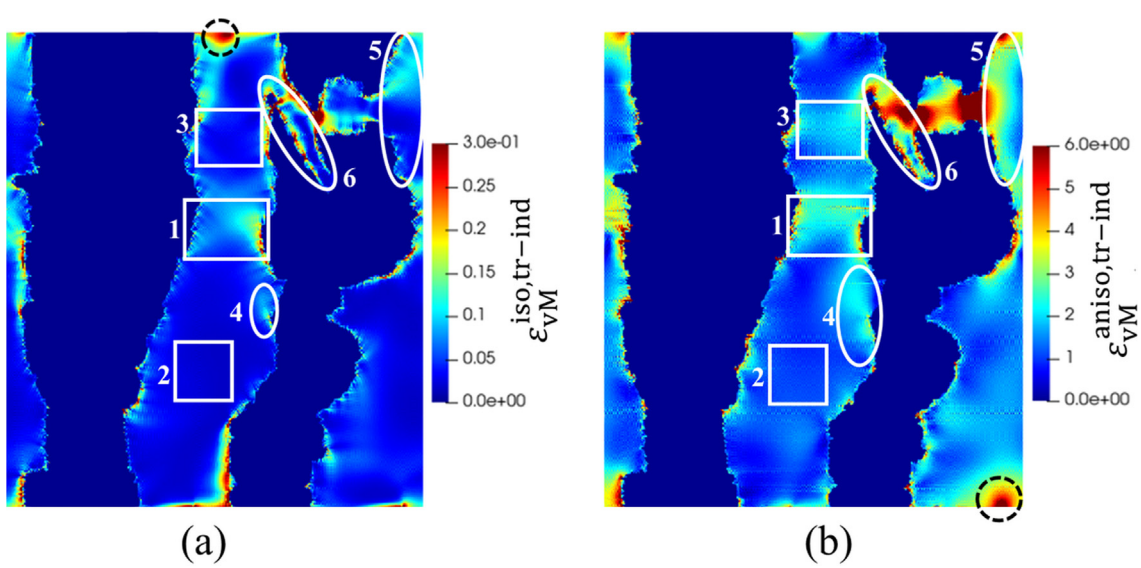

Fig. 6. von-Mises equivalent map of (a) transformation-induced strain in ferrite due to isotropic transformation eigenstrains, $\epsilon_{vM}^{iso,tr\text{-}ind}$, and (b) transformation-induced strain in ferrite due to anisotropic transformation eigenstrains, $\epsilon_{vM}^{aniso,tr\text{-}ind}$.

transformation-induced deformation of ferrite is not only because of complex grain shapes but also because of the variants formed within PAGs. This is because the magnitude and direction of shear and dilatation deformation are different for every martensitic variant. As a consequence, every variant uniquely deforms the surrounding ferrite matrix.

On comparing the results of the present micromechanical model calculations to the GND density map, it is observed that the regions of high GND density marked 'II', 'III', and 'IV' in Fig. 2(f) correspond to the regions of high strain '4', '6', and 'respectively in Figs. 6(a) and (b). This correspondence is stronger in Fig. 6(b), i.e., in the case of anisotropic transformation. There are also some regions of high GND density, such as the one marked 'I' in Fig. 2(f), which do not have high strain at the corresponding locations in the strain maps. This is perhaps because the transformation-induced deformation of ferrite observed on the surface is also contributed to by the martensite formation below the observed surface, while the present study is carried out on a 2D EBSD-based RVE. Region '3' with high strain in Fig. 6(b) does not have a corresponding region of high GND density in Fig. 2(f).

This study elucidates the importance of including the anisotropy of martensitic transformation deformation in modeling the mechanical behavior of DP steels. However, it also reveals that indirect measures of in-grain deformation in the form of experimental KAM or GND values are insufficient to validate transformation-induced deformation of ferrite estimated via current modeling approach. Hence, the following aspects of this study can be considered in future investigations: (i) Instead of PTMC, more advanced theories such as the double shear theory [47] and parameter-free double shear theory [48] can be used to calculate anisotropic transformation strains with even more accuracy, (ii) the local variations in the carbon content of the martensite should be taken into account while using PTMC and PAG reconstruction, (iii) 3D PAG reconstruction based on 3D EBSD measurement should be carried out to take into account the anisotropic transformation strains associated with martensite formation beneath the observed surface, (iv) The use of finite strain definition in micromechanical calculations should provide more accurate quantification of transformation-induced strains in ferrite.

5. Conclusions

The martensitic transformation-induced deformation of ferrite has a profound effect on the mechanical behavior of DP steels. In previous studies modeling the transformation-induced deformation of ferrite, the anisotropy of transformation deformation was ignored. Rather, isotropic dilatation alone was considered to induce the deformation of surrounding ferrite matrix. In this work, the validity of the assumption of isotropic dilatation during transformation of small PAGs and the effect of anisotropic transformation deformation in causing deformation of surrounding ferrite matrix in DP steels is evaluated.

To this end, a methodology is developed whereby the martensitic transformation-induced strains can be studied in DP steels as well as other multiphase steel microstructures containing martensite. The methodology includes four steps: (i) Analysis of the ferrite/martensite dual-phase microstructure, (ii) prior austenite grain reconstruction (iii) determination of martensitic transformation deformation, and (iv) calculation of transformation-induced strains in the ferrite matrix surrounding the martensite.

In previous modeling works concerning the transformation-induced deformation of ferrite in DP steels, PAG orientations were disregarded. In this study, the PAG orientations and morphology are obtained via PAG reconstruction from martensite regions of DP steel microstructure. The results of the PAG reconstruction and PTMC are then combined with the EBSD orientation data for the martensite in a unique way to estimate variant-specific transformation deformation required for performing micromechanical calculations. The calculated transformation-induced strains in ferrite are further compared with experimental EBSD KAM and GND measurements of the same.

The results show regions of relatively large deformation in ferrite very close to the phase boundaries in experimental EBSD KAM and GND density maps as well as simulated ferrite strain maps. However, not all regions of large deformation in experimental and simulated results necessarily coincide. The assumption of isotropic or anisotropic transformation deformation in the micromechanical calculations affects the distribution of transformation-induced strains in ferrite. The transformation-induced deformation of ferrite is determined primarily by prior austenite and ferrite grain shapes along with the anisotropy of martensitic transformation deformation. It is also shown that neglecting the shear deformation associated with martensitic transformation under the assumption of isotropic dilatation results in significant underestimation of transformation-induced strains in ferrite.

CRediT authorship contribution statement

Vibhor Atreya: Conceptualization, Methodology, Software, Validation, Formal analysis, Investigation, Writing – original draft, Visualization. **Jan Steven Van Dokkum:** Methodology, Software, Formal analysis, Writing – review & editing. **Cornelis Bos:** Writing – review & editing, Supervision, Project administration. **Maria J. Santofimia:** Writing – review & editing, Supervision, Project administration.

Data availability

The raw and processed data required to reproduce these findings are available to download from: https://doi.org/10.4121/19411379.

Declaration of Competing Interest

The authors declare that they have no known competing financial interests or personal relationships that could have appeared to influence the work reported in this paper.

Acknowledgements

This research was carried out under project number T17019j in the framework of the Research Program of the Materials innovation institute (M2i) (www.m2i.nl) supported by the Dutch government.

Appendix A

A.1. The micromechanical model

The macroscopic behavior of a homogenized elastic composite is given as:

$$S = \mathscr{C} : E, \tag{A.1}$$

where $\mathscr{C}$ is the effective elastic moduli, S and E are the averages of stress field, $\boldsymbol{\sigma}(x)$, and strain field, $\boldsymbol{\epsilon}(x)$, respectively, which are computed as the solution of following problem:

$$\begin{cases} \boldsymbol{\sigma}(x) = \mathscr{C}^{\mathrm{r}} : \boldsymbol{\epsilon}(x), & \\ \boldsymbol{\epsilon}(x) = \boldsymbol{\epsilon}(u^{+}(x)) + E\,, & \forall x \in V \\ \nabla \cdot \boldsymbol{\sigma}(x) = 0\,, & \forall x \in V \\ u^{+} \text{ is periodic}\,, & \boldsymbol{\sigma} : \hat{n} \text{is anti-periodic}\,, \end{cases} \tag{A.2}$$

where $\mathscr{C}^{\mathrm{r}}$ is the elastic moduli tensor in phase $r, \boldsymbol{\epsilon}(u^{+}(x))$ is the polarization field of strain and V is the periodic volume. To solve set of Eqs. A.2, a fast fourier transform (FFT) based method is developed by H. Moulinec and P. Suquet [24] is used. The Problem A.2 is then replaced by an auxiliary problem which includes a linear homogenous elastic body of stiffness $\mathscr{C}^{0}$ under a polarization field $\boldsymbol{\tau}(x)$.

$$\begin{cases} \boldsymbol{\sigma}(x) = \mathscr{C}^{0} : \boldsymbol{\epsilon}(x) + \boldsymbol{\tau}(x), & \\ \boldsymbol{\tau}(x) = \left(\mathscr{C}^{r} - \mathscr{C}^{0}\right) : \boldsymbol{\epsilon}(x), & \\ \boldsymbol{\epsilon}(x) = E - \Gamma^{0} * \boldsymbol{\tau}(x), & \forall x \in V \\ \nabla \cdot \sigma(x) = 0\,, & \forall x \in V \\ u^{+} \text{ is periodic}, & \boldsymbol{\sigma} : \hat{n} \text{ is anti-periodic}\,, \end{cases} \tag{A.3}$$

with the periodic Green's operator Γ^{0} associated with $\mathscr{C}^{0}$ and * the convolution product. The Γ^{0} operator is explicitly known in fourier space. In the current work, $\boldsymbol{\epsilon}(x)$ is initialized with values of transformation eigenstrains for martensitic variants $\boldsymbol{\epsilon}^{*}(x)$. The isotropic transformation eigenstrain, $\boldsymbol{\epsilon}^{*,\mathrm{iso}}$ is given by $(\delta/3)\,\boldsymbol{\epsilon}_{ii}$, where δ is given by Eq. 11, while anisotropic transformation eigenstrains are calculated from deformation gradient matrix $\mathbf{Z}$ obtained via PTMC theory using the definition of Green-Lagrange strain:

$$\boldsymbol{\epsilon}^{*,\mathrm{aniso}}(x) = \frac{1}{2}\left[\mathbf{Z}(x)^{\mathrm{T}} \cdot \mathbf{Z}(x) - \mathrm{I}\right], \tag{A.4}$$

where I is the identity matrix. Subsequently, $\boldsymbol{\epsilon}^{*}(x)$ is used to calculate the polarization field $\boldsymbol{\tau}(x)$ which is held constant. Problem A.3 is then solved iteratively. The convergence is reached when error e is below a specified value:

$$e = \frac{\left(\left\langle \|\nabla \cdot \sigma\|^{2} \right\rangle\right)^{\frac{1}{2}}}{\|\langle \sigma \rangle\|}\,, \tag{A.5}$$

The elastic-plastic von-Mises materials obey the following linear hardening law:

$$\begin{cases} \boldsymbol{\sigma} = \mathscr{C}^{\mathrm{r}}\left(\boldsymbol{\epsilon} - \boldsymbol{\epsilon}_{\mathrm{p}}\right), & \\ \dot{\boldsymbol{\epsilon}}_{\mathrm{p}} = \frac{3}{2}\,\dot{p}\,\frac{\boldsymbol{\sigma}_{\mathrm{d}}}{\boldsymbol{\sigma}_{\mathrm{vM}}} \;\text{ where }\; p = \frac{2}{3}\sqrt{\boldsymbol{\epsilon}_{\mathrm{p}} \cdot \boldsymbol{\epsilon}_{\mathrm{p}}}\,, & \\ \sigma_{\mathrm{vM}} \geqslant \sigma_{\mathrm{Y}}\,, & \end{cases} \tag{A.6}$$

where $\boldsymbol{\epsilon}_{\mathrm{p}}$ is the deviatoric plastic strain, $\boldsymbol{\sigma}_{\mathrm{d}}$ and σ_{vM} are the deviatoric stress and von-Mises equivalent stress respectively, p is the hardening parameter and σ_{Y} is the yield strength.

References

[1] T. Matsuno, R. Ando, N. Yamashita, H. Yokota, K. Goto, I. Watanabe, Analysis of preliminary local hardening close to the ferrite–martensite interface in dual-phase steel by a combination of finite element simulation and nanoindentation test, Int. J. Mech. Sci. 180 (March) (2020).

[2] F. Badkoobeh, H. Mostaan, M. Rafiei, H.R. Bakhsheshi-Rad, F. Berto, Microstructural Characteristics and Strengthening Mechanisms of Ferritic–Martensitic Dual-Phase Steels: A Review, Metals 12 (1) (2022).

[3] S. Li, C. Guo, L. Hao, Y. Kang, Y. An, Microstructure-Based Modeling of Mechanical Properties and Deformation Behavior of DP600 Dual Phase Steel, Steel Res. Int. 90 (12) (2019) 1–10.

[4] J.M. Moyer, G.S. Ansell, The Volume Expansion Accompanying the Martensite Transformation in Iron-Carbon Alloys, Metall. Trans. A 6A (September) (1975) 1785–1791.

[5] J.S. Bowles, J.K. Mackenzie, The crystallography of martensite transformations I, Acta Metall. 2 (1) (1954) 129–137.

[6] A. Ramazani, K. Mukherjee, U. Prahl, W. Bleck, Transformation-induced, geometrically necessary, dislocation-based flow curve modeling of dual-phase steels: Effect of grain size, Metall. Mater. Trans. A 43 (10) (2012) 3850–3869.

[7] A. Ramazani, K. Mukherjee, A. Schwedt, P. Goravanchi, U. Prahl, W. Bleck, Quantification of the effect of transformation-induced geometrically necessary dislocations on the flow-curve modelling of dual-phase steels, Int. J. Plast. 43 (2013) 128–152.

[8] U. Liedl, S. Traint, E.A. Werner, An unexpected feature of the stress-strain diagram of dual-phase steel, Comput. Mater. Sci. 25 (1–2) (2002) 122–128.

[9] D.A. Korzekwa, D.K. Matlock, G. Krauss, Dislocation substructure as a function of strain in a dual-phase steel, Metall. Trans. A 15 (6) (1984) 1221–1228.

[10] S. Li, C. Guo, L. Hao, Y. Kang, Y. An, In-situ EBSD study of deformation behaviour of 600 MPa grade dual phase steel during uniaxial tensile tests, Mater. Sci. Eng., A 759 (March) (2019) 624–632.

[11] T. Sakaki, K. Sugimoto, T. Fukuzato, Role of Internal Stress for the Initial Yielding of Dual-Phase Steels, Acta Metall. 31 (10) (1983) 1737–1746.

[12] D.L. Bourell, A. Rizk, Influence of martensite transformation strain on the ductility of dual-phase steels, Acta Metall. 31 (4) (1983) 609–617.

[13] C.C. Tasan, M. Diehl, D. Yan, M. Bechtold, F. Roters, L. Schemmann, C. Zheng, N. Peranio, D. Ponge, M. Koyama, K. Tsuzaki, D. Raabe, An Overview of Dual-Phase Steels: Advances in Microstructure-Oriented Processing and Micromechanically Guided Design, Annu. Rev. Mater. Res. 45 (2015) 391–431.

[14] R.G. Davies, Early Stages of Yielding and Strain Aging of a, Metall. Trans. A 10A (1979).

[15] M. Calcagnotto, D. Ponge, E. Demir, D. Raabe, Orientation gradients and geometrically necessary dislocations in ultrafine grained dual-phase steels studied by 2D and 3D EBSD, Mater. Sci. Eng., A 527 (10–11) (2010) 2738–2746.

[16] R. Ando, T. Matsuno, T. Matsuda, N. Yamashita, H. Yokota, K. Goto, I. Watanabe, Analysis of nano-hardness distribution near the ferritemartensite interface in a dual phase steel with factorization of its scattering behavior, ISIJ Int. 61 (1) (2021) 473–480.

[17] H. Ashrafi, M. Shamanian, R. Emadi, M. Sanayei, F. Farhadi, J.A. Szpunar, Characterization of Microstructure and Microtexture in a Cold-Rolled and Intercritically Annealed Dual-Phase Steel, J. Mater. Eng. Perform. 30 (10) (2021) 7306–7313.

[18] J. Kadkhodapour, S. Schmauder, D. Raabe, S. Ziaei-Rad, U. Weber, M. Calcagnotto, Experimental and numerical study on geometrically necessary dislocations and non-homogeneous mechanical properties of the ferrite phase in dual phase steels, Acta Mater. 59 (11) (2011) 4387–4394.

[19] C. Du, J.P. Hoefnagels, S. Kölling, M.G. Geers, J. Sietsma, R. Petrov, V. Bliznuk, P. M. Koenraad, D. Schryvers, B. Amin-Ahmadi, Martensite crystallography and chemistry in dual phase and fully martensitic steels, Mater. Characteriz. 139 (October 2017) (2018) 411–420.

[20] S. Takaki, K. Fukunaga, J. Syarif, T. Tsuchiyama, Effect of Grain Refinement on Thermal Stability of Metastable Austenitic Steel, Mater. Trans. 45 (7) (2004).

[21] C. Celada-Casero, J. Sietsma, M.J. Santofimia, The role of the austenite grain size in the martensitic transformation in low carbon steels, Mater. Des. 167 (2019).

[22] J.S. Bowles, J.K. Mackenzie, The crystallography of martensite transformations III. Face-centred cubic to body-centred tetragonal transformations, Acta Metall. 2 (2) (1954) 224–234.

[23] C.M. Wayman, The phenomenological theory of martensite crystallography: Interrelationships, Metall. Mater. Trans. A 25 (9) (1994) 1787–1795.

[24] H. Moulinec, P. Suquet, A numerical method for computing the overall response of nonlinear composites with complex microstructure, Comput. Methods Appl. Mech. Eng. 157 (1–2) (1998) 69–94.

[25] L. Ryde, Application of EBSD to analysis of microstructures in commercial steels Application of EBSD to analysis of microstructures in commercial steels, Mater. Sci. Technol. 836 (2006).

[26] G. Miyamoto, N. Takayama, T. Furuhara, Accurate measurement of the orientation relationship of lath martensite and bainite by electron backscatter diffraction analysis, Scripta Mater. 60 (12) (2009) 1113–1116.

[27] T. Nyyssönen, M. Isakov, P. Peura, V.T. Kuokkala, Iterative Determination of the Orientation Relationship Between Austenite and Martensite from a Large Amount of Grain Pair Misorientations, Metall. Mater. Trans. A: Phys. Metall. Mater. Sci. 47 (6) (2016) 2587–2590.

[28] T. Nyyssönen, P. Peura, V.T. Kuokkala, Crystallography, Morphology, and Martensite Transformation of Prior Austenite in Intercritically Annealed High-Aluminum Steel, Metall. Mater. Trans. A 49 (12) (2018) 6426–6441.

[29] H. Bhadeshia, Worked Examples in the Geometry of Crystals, second ed., The institute of Metals, London, 1991.

[30] P.M. Kelly, J. Nutting, The martensite transformation in carbon steels, Proc. Roy. Soc. Lond. Ser. A. Math. Phys. Sci. 259 (1296) (1960) 45–58.

[31] Z. Nishiyama, Martensitic Transformation, Academic Press, Inc., 1972.

[32] X.F. Gu, T. Furuhara, W.Z. Zhang, PTCLab: Free and open-source software for calculating phase transformation crystallography, J. Appl. Crystallogr. 49 (April) (2016) 1099–1106.

[33] H. Kitahara, R. Ueji, M. Ueda, N. Tsuji, Y. Minamino, Crystallographic analysis of plate martensite in Fe-28.5 at.% Ni by FE-SEM/EBSD, Mater. Charact. 54 (4–5) (2005) 378–386.

[34] H. Kitahara, R. Ueji, N. Tsuji, Y. Minamino, Crystallographic features of lath martensite in low-carbon steel, Acta Mater. 54 (5) (2006) 1279–1288.

[35] L. Sharma, R.H. Peerlings, M.G. Geers, F. Roters, Microstructural influences on fracture at prior austenite grain boundaries in dual-phase steels, Materials 12 (22) (2019) 1–22.

[36] V. Atreya, C. Bos, M.J. Santofimia, Understanding ferrite deformation caused by austenite to martensite transformation in dual phase steels, Scripta Mater. 202 (2021) 114032.

[37] V.A. Lobodyuk, Y.Y. Meshkov, E.V. Pereloma, On Tetragonality of the Martensite Crystal Lattice in Steels, Metall. Mater. Trans. A 50 (1) (2019) 97–103.
[38] M. Kamaya, Assessment of local deformation using EBSD: Quantification of accuracy of measurement and definition of local gradient, Ultramicroscopy 111 (8) (2011) 1189–1199.
[39] F. Bachmann, R. Hielscher, H. Schaeben, Texture analysis with MTEX- Free and open source software toolbox, Solid State Phenom. 160 (2010) 63–68.
[40] R. Hielscher, T. Nyyssönen, F. Niessen, A.A. Gazder, The variant graph approach to improved parent grain reconstruction, Materialia 22 (March) (2022) 101399.
[41] F. Niessen, T. Nyyssönen, A.A. Gazder, R. Hielscher, Parent grain reconstruction from partially or fully transformed microstructures in MTEX, J. Appl. Crystallogr. 55 (2022) 180–194.
[42] W. Pantleon, Resolving the geometrically necessary dislocation content by conventional electron backscattering diffraction, Scripta Mater. 58 (11) (2008) 994–997.
[43] A.H. Pham, T. Ohba, S. Morito, T. Hayashi, Effect of Chemical Composition on Average γ/α' Orientation Relationship in Carbon and Low Alloy Steels, Mater. Today: Proc. 2 (2015) S663–S666.
[44] A. Saha Podder, H.K. Bhadeshia, Thermal stability of austenite retained in bainitic steels, Mater. Sci. Eng., A 527 (7–8) (2010) 2121–2128.
[45] R.-M. Rodriguez, I. Gutiérrez, Unified Formulation to Predict the Tensile Curves of Steels with Different Microstructures, Mater. Sci. Forum 426–432 (2003) 4525–4530.
[46] S.A. Kim, W.L. Johnson, Elastic constants and internal friction of martensitic steel, ferritic-pearlitic steel, and α-iron, Mater. Sci. Eng. A 452–453 (2007) 633–639.
[47] P.M. Kelly, Crystallography of lath martensite in steels, Mater. Trans. JIM 33 (3) (1992) 235–242.
[48] F. Maresca, W.A. Curtin, The austenite/lath martensite interface in steels: Structure, athermal motion, and in-situ transformation strain revealed by simulation and theory, Acta Mater. 134 (2017) 302–323.